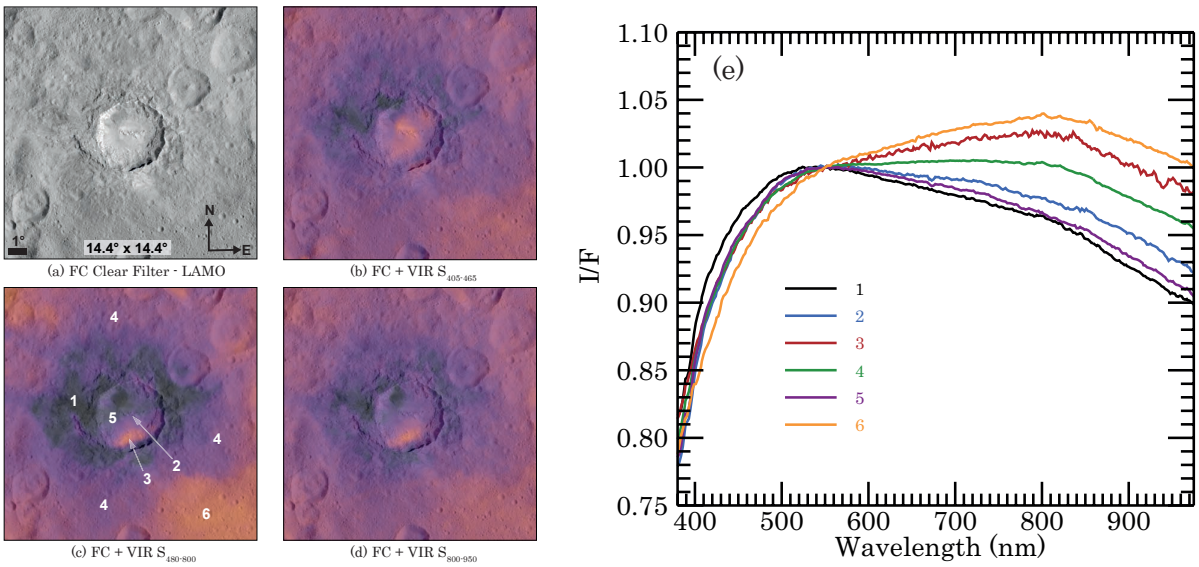

Fig. 11. Same as Fig. 8 for Haulani. Haulani has a diameter of 34 km. All the images use a spherical projection with a field of 14.4° × 14.4° and have the same orientation.

and the Oxo and Kupalo craters – with $I/F_{550\mathrm{nm}}$ reaching 0.050 on the central peak. Furthermore, we note that the $I/F_{550\mathrm{nm}}$ of the crater floor is relatively well correlated with the $I/F_{1.2\mu\mathrm{m}}$ and the $I/F_{1.9\mu\mathrm{m}}$ while on the ejecta, compared to the Ceres average, the $I/F_{550\mathrm{nm}}$ is brighter and both the $I/F_{1.2\mu\mathrm{m}}$ and the $I/F_{1.9\mu\mathrm{m}}$ are darker (Ciarniello et al. 2017; Tosi et al. 2018, 2019). If not the brightest, Haulani is the bluest feature of the surface, as illustrated by Figs. 3 and 4, and already noted by Nathues et al. (2016), Stephan et al. (2017), Schröder et al. (2017) and Tosi et al. (2018, 2019). This argues for the very young age of its formation (Stephan et al. 2017).

The three spectral slopes mapped in Fig. 11 present different characteristics, the $S_{405-465\mathrm{nm}}$ showing a different spatial distribution when compared with the $S_{480-800\mathrm{nm}}$ and $S_{800-950\mathrm{nm}}$ slopes, which are more similar to each other. The northern, western, and eastern rims of Haulani and the associated ejecta blanket (area and spectrum n°1 of Fig. 11) show the lowest value of the slope $S_{405-465\mathrm{nm}}$ of the features presented in Sect. 4, with a value as low as 1.49×10^{-4} kÅ^{-1}. The crater floor exhibits higher $S_{405-465\mathrm{nm}}$ (around 1.90×10^{-4} kÅ^{-1}), which are mainly correlated with the central peak, but nevertheless encompass a larger area that includes the south of the crater floor and a small patch on the northeastern talus material (see area and spectrum n°2).

The ejecta of Haulani, mostly westward-oriented, are adequately visible in the spectral slope maps (Figs. 5–7), and, in $S_{480-800\mathrm{nm}}$, show the largest contrast with respect to the surrounding terrains. Those latter are represented by the area and the spectrum n°6 in Fig. 11, have a slope $S_{480-800\mathrm{nm}}$ around 1.65×10^{-5} kÅ^{-1}. Conversely, the closest to the crater and bluest ejecta (n°1), as well as the one a bit farther (n°4), exhibit $S_{480-800\mathrm{nm}}$ around -6.42×10^{-6} kÅ^{-1} and 9.58×10^{-6} kÅ^{-1}, respectively.

Haulani crater's floor presents interesting features revealed by the spectral slopes $S_{480-800\mathrm{nm}}$ and $S_{800-950\mathrm{nm}}$. The north, illustrated by the spectrum n°5 on Fig. 11, shows a patch as blue as the bluest ejecta n°1. This patch corresponds to the "crater floor material smooth dark" (or cfsd unit), as mapped by Krohn et al. (2018). On the opposite side of the crater floor (area n°3), the $S_{480-800\mathrm{nm}}$ and $S_{800-950\mathrm{nm}}$ slopes are higher, reaching values of 1.65×10^{-5} kÅ^{-1} and -2.29×10^{-5} kÅ^{-1}, respectively, which means relatively close to the surrounding area n°6. This peculiar zone (area n°3) corresponds to the "crater floor material hummocky bright" (or cfhb unit), as mapped by Krohn et al. (2018) and which probably corresponds to material fallen down from the crater rims which are steeper on this side of the crater (Krohn et al. 2018).

The Haulani crater, revealed through our spectral indices, can be compared with the composition maps that have already been published. We first note that no obvious correlation is observed between our spectral slopes and the carbonates distribution around Haulani (Carrozzo et al. 2018; Tosi et al. 2019). However, a good qualitative correspondence can be drawn between the more negative $S_{480-800\mathrm{nm}}$ slope and the lower band depth at 2.7 and 3.1 μm (Ammannito et al. 2016; Tosi et al. 2019). A good qualitative correlation is also observed between the $S_{480-800\mathrm{nm}}$ and $S_{800-950\mathrm{nm}}$ slopes on area n°3 and the 2.7 μm band depth, but less with the 3.1 μm band depth (Tosi et al. 2018, 2019). Finally, the visible spectral slopes, $S_{480-800\mathrm{nm}}$ and $S_{800-950\mathrm{nm}}$, are correlated with the infrared spectral slope, at least in the area n°3 and with the ejecta in general (Tosi et al. 2018, 2019).

4.5. Juling and Kupalo

Juling and Kupalo are two neighbor craters of 20 and 26 km in diameter; Kupalo, south of Juling, is younger. The analysis of the spectral diversity with our data is difficult due to the sparse coverage of this area. This is visible as white irregular dots on the spectral slope maps and noisy spectra in Fig. 12.

While the context of Juling and Kupalo is very rich in detail (e.g., Stephan et al. 2017; De Sanctis et al. 2019), the visible spectral indices do not show a huge diversity. One remarkable area is the floor of Juling (area and spectrum n°1), which stands out in the $S_{480-800\mathrm{nm}}$ and $S_{800-950\mathrm{nm}}$ maps and has spectral slopes similar to the terrain outside the ejecta (area and spectrum n°5) with values around 2.48×10^{-5} kÅ^{-1} and 2.65×10^{-5} kÅ^{-1} for the $S_{480-800\mathrm{nm}}$ and around -1.68×10^{-5} kÅ^{-1} and -1.92×10^{-5} kÅ^{-1} for the $S_{800-950\mathrm{nm}}$, respectively. However, the reflectance of the two areas are quite different, with the Juling crater floor having a median $I/F_{550\mathrm{nm}}$ around 0.039, while the area n°5 close to 0.034, is similar to the mean of Ceres.

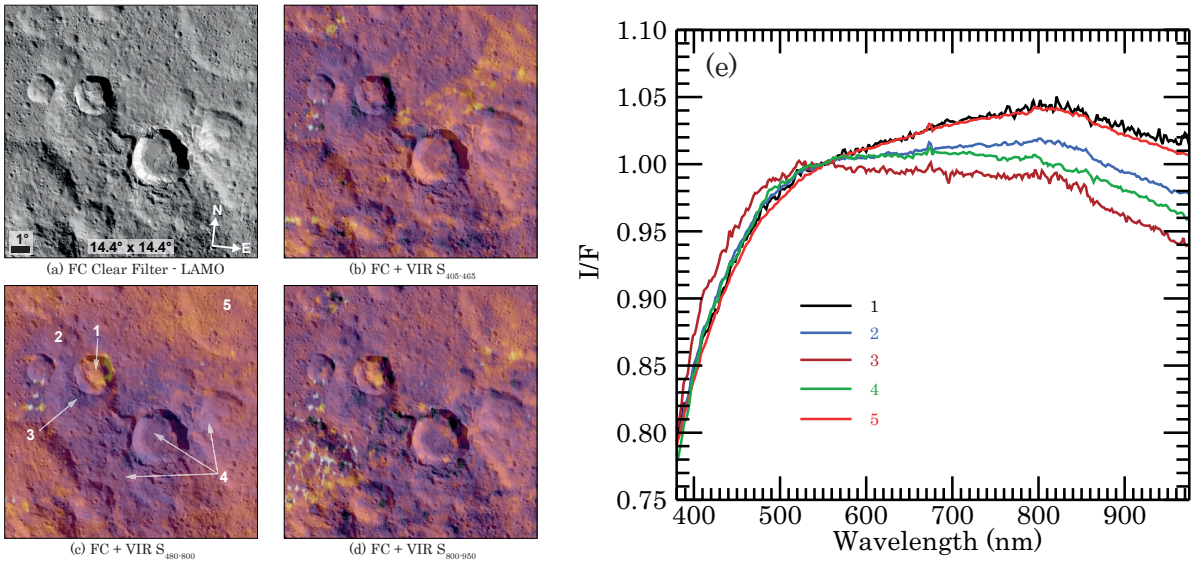

Fig. 12. Same as Fig. 8 for Juling and Kupalo. Juling and Kupalo have diameters of 20 and 26 km, respectively. All the images use a spherical projection with a field of 14.4° × 14.4° and have the same orientation.

One recurrent feature observed in the three spectral slopes is a patch in the south west ejecta blanket of Juling, designated as area n°3. This area has the lowest values of each slope in Fig. 12 ($S_{405-465nm} \simeq 1.56 \times 10^{-4}$ kÅ^{-1}, $S_{480-800nm} \simeq 3.16 \times 10^{-6}$ kÅ^{-1}, and $S_{800-950nm} \simeq -3.06 \times 10^{-5}$ kÅ^{-1}).

Kupalo, in addition to being bright like Juling (median I/F_{550nm} of 0.040), appears blue in the maps of Figs. 3 and 4, and as also pointed out by e.g., Nathues et al. (2016) and Stephan et al. (2017). The low value of the slope $S_{480-800nm}$ (1.25×10^{-5} kÅ^{-1}) of the Kupalo crater floor and its ejecta (area n°4) corresponds to a mostly flat spectrum beyond 500 nm. This is still bluer than the Juling ejecta (area and spectrum n°2) which exhibit $S_{480-800nm}$ around 1.53×10^{-5} kÅ^{-1}.

Carbonates have been detected all around the Kupalo crater with the higher abundance in the south-west part (Carrozzo et al. 2018). On the contrary, the band depths at 2.7 and at 3.1 μm are lower in those places, as shown by Ammannito et al. (2016) and De Sanctis et al. (2019). However, in both cases, we do not observe a peculiar spectral behavior at VIS wavelengths.

4.6. Occator

Occator (92 km in diameter) is one of the most interesting and intriguing craters of Ceres. Its peculiarity, as visible in Fig. 13, is attributed to two very bright spots, or faculae, of endogenous origin and which have been tentatively observed in some pre-Dawn Ceres observations (Li et al. 2006; Carry et al. 2008). The origin and the formation of Occator have been abundantly discussed (see Scully et al. 2019 and references within). Concerning the central bright spot – the complex Cerealia facula and dome – the latest VIR IR observations suggests the presence of hydrated sodium chloride, which would have been able to lower the eutectic temperature of different materials beneath the surface, favoring the ascent of fluids (De Sanctis et al. 2020).

As for the other cases studied in this section, the $S_{480-800nm}$ slope shows the most evident variations. At a larger scale (see Fig. 6), a system of curved ejecta rays is particularly visible in the southwest-southeast. The farthest ejecta formed a circular to elliptical light violet area around the crater, where the slope is slightly positive to null. Closest to the crater and based on our spectral slope definitions, we identified six areas of different spectral behaviors. The area n°2, while still on the ejecta, represents the surroundings of the crater and has a value of the $S_{480-800nm}$ around 2.27×10^{-5} kÅ^{-1}. The slope decreases on the ejecta blanket, in particular on the west and southwest sides (area and spectrum n°4) where $S_{480-800nm}$ is about 8.19×10^{-6} kÅ^{-1}. The area n°6, which is defined as a large annular ring (excluding area n°4), exhibits spectral behavior between the area n°2 and n°4. The Occator crater floor (area and spectrum n°5) has the lowest values of $S_{480-800nm}$, being around 4.78×10^{-6} kÅ^{-1}. Area n°3 corresponds to a part of the rim and the outer ejecta blanket where $S_{480-800nm}$ is a bit higher, reaching a value of 2.17×10^{-5} kÅ^{-1}, close to the surrounding terrains' $S_{480-800nm}$ values. Area n°3 is also slightly visible through the $S_{800-950nm}$ indicator, and it is interesting to note that Raponi et al. (2019b) reports a higher abundance of Mg-phyllosilicates and Mg-carbonates in that area.

Spectral slopes, $S_{405-465nm}$ and $S_{800-950nm}$, do not present important variations at this scale on Occator, except on the faculae. The southwest-northeast-oriented line across the Occator crater floor and crossing the Cerealia facula, only visible on the $S_{405-465nm}$ and $S_{800-950nm}$ maps as a low values area, is likely a smearing artifact associated to the high signal acquired on the facula. The crater floor and the closest ejecta (areas n°3, n°4 and n°5) have one of the lowest $S_{405-465nm}$ values of Ceres (1.60×10^{-4} kÅ^{-1} < $S_{405-465nm}$ < 1.64×10^{-4} kÅ^{-1}). As illustrated by the map of I/F_{550nm} in Fig. 2, the variation in reflectance is very important at Occator. On Cerealia facula, the I/F_{550nm} reaches a median of 0.19 at 550 nm, with a maximum as high as 0.26 for some observations. For comparison, the I/F_{550nm} of the nearby Vinalia facula is around 0.10 for the brightest observations, while values for Haulani or Oxo reach 0.07. On the contrary, the ejecta located on the northern part have one of the lowest I/F_{550nm}, around 0.030 for areas n°2 and n°3. At this location Raponi et al. (2019b) report a higher abundance of NH4-phyllosilicates and, while it is not necessarily intuitive, a lower abundance of dark material.

On the Occator faculae, the combination between the brightness of the faculae and the integration time leads to an incorrect response of the VIS detector. For this reason, the dataset used

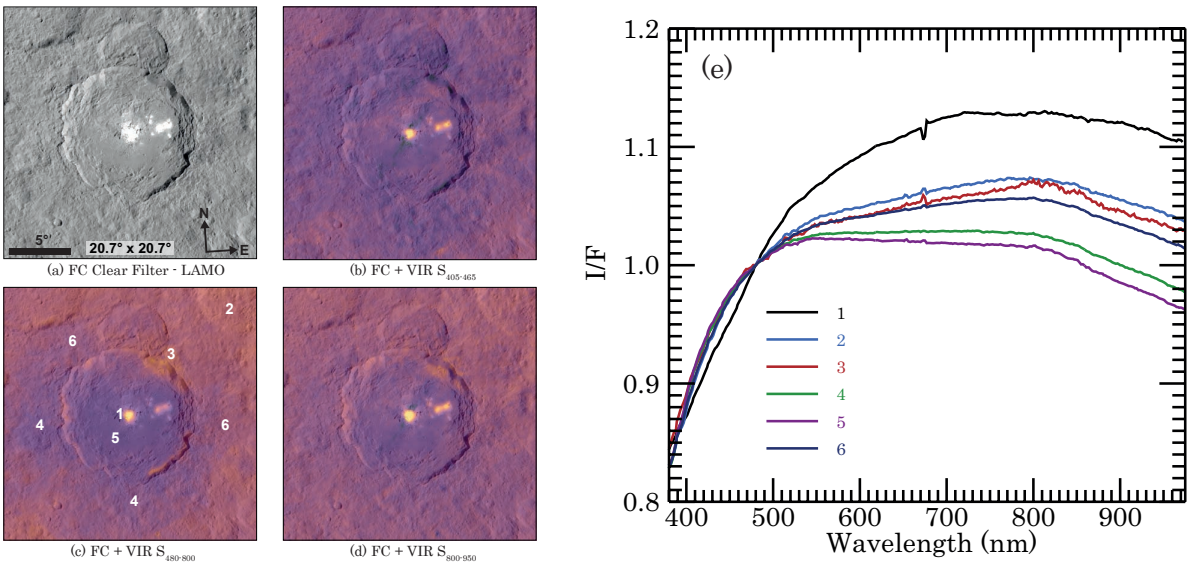

Fig. 13. Same as Fig. 8 for Occator. Occator has a diameter of 92 km. All the images use a spherical projection with a field of 20.7° × 20.7° and have the same orientation.

here does not allow for a properly study of the faculae. In order to obtain a reliable spectrum, we use a cube (524703945) which is less affected by artifacts acquired during the Ceres Extended Low Altitude Mapping Orbit (CXL) mission phase. Figure 13 includes the spectrum extracted from this cube (n°1) and is relative to the Cerealia facula. Vinalia facula is not covered in the cube. The spectrum n°1 has a different global shape, compared to the other one already discussed. While the $S_{405-465nm}$ is not extreme (around 1.76×10^{-4} kÅ^{-1}), this part of the spectrum is straighter, and it extends up to larger wavelengths. On the contrary, while most of the Ceres spectra have a $S_{480-800nm}$ relatively straight after 500 nm, the spectrum of Cerealia facula is much more curved on this range. This does not prevent the $S_{480-800nm}$ to be the highest observed on Ceres, with a value as high as 4.03×10^{-5} kÅ^{-1}. This is almost two times the value of the area n°2 and higher than for Ernutet's organic rich terrain, which reaches 3.39×10^{-5} kÅ^{-1}. The slope, $S_{800-950nm}$, is also high on the faculae, around -1.19×10^{-5} kÅ^{-1} (-6.47×10^{-6} kÅ^{-1} on Ernutet for example).

To establish a link between the composition or the state of the surface through the visible spectral indices on the faculae of Occator is not easy. Sodium carbonates are present on the faculae (De Sanctis et al. 2016; Carrozzo et al. 2018), as well as ammonia-bearing and sodium chloride species – but to a lesser extent (De Sanctis et al. 2016, 2020; Ammannito et al. 2016; Raponi et al. 2019b). While the spectral shape of the VIS spectrum and its associated slopes and reflectance values are undoubtedly influenced by this peculiar composition, it is not possible to distinguish the separate effect of each component.

4.7. Oxo

Oxo is a 10 km-diameter, geologically young crater located at 0°E-45°N. The ejecta of Oxo are poorly extended and among the three spectral slopes – $S_{405-465nm}$, $S_{480-800nm}$, and $S_{800-950nm}$ – only $S_{480-800nm}$ is well correlated with those ejecta, as illustrated in Fig. 14. The crater floor exhibits a spectral behavior similar to the closest ejecta, and both those areas have been merged in the spectra n°1 of Fig. 14. The $S_{480-800nm}$ slope of this area shows one of the lowest values on the surface of Ceres – reaching $S_{480-800nm} \simeq 8,49 \times 10^{-7}$ kÅ^{-1} – while the surrounding area and spectrum n°3 are typical of the major part of the Ceres surface, with a value of about $S_{480-800nm} \simeq 2.07 \times 10^{-5}$ kÅ^{-1}. A distinct gradation is visible through the $S_{480-800nm}$ slope between the crater floor and the closest ejecta (n°1 on Fig. 14), the surrounding terrain (n°3), and farther ejecta from the crater (spectra and area n°2).

The slopes $S_{405-465nm}$ and $S_{800-950nm}$ on the ejecta exhibit values very close to the surrounding terrains even if some heterogeneities are still visible. However, the level of variation does not allow us to draw any conclusions about the genuineness and significance of the small variations.

As seen in the FC image of Fig. 14, the Oxo crater and its ejecta are particularly bright. Our VIR observations report a reflectance I/F_{550nm} around 0.047 for the area n°1, while the area n°3 is around 0.035. As reported by Combe et al. (2016), the signature of water ice has been identified on the south rim of Oxo. The VIR observations in the visible area of the same pixels do not allow for a peculiar spectral behavior to be highlighted and they are not reported nor discussed here. Carrozzo et al. (2018) report a high abundance of carbonates in Oxo. While this high concentration could correlate with a lower $S_{465-800nm}$ spectral slope in the northern ejecta and the crater floor, this is not the case in the southwestern part, where the carbonate concentration is also high.

5. General discussion

In this section, we focus our interest on the global maps presented in Sect. 3. The spectrum of the sunlight reflected by a surface is the result of a combination of the surface mineralogy along with several physical effects and processes acting on the surface. At visible wavelengths, the Ceres spectrum is devoid of any complete absorption band. Nevertheless, we used several spectral indices – reflectance, colors, color ratio, and spectral slopes – to characterize the surface of Ceres and observe the variations of its properties.

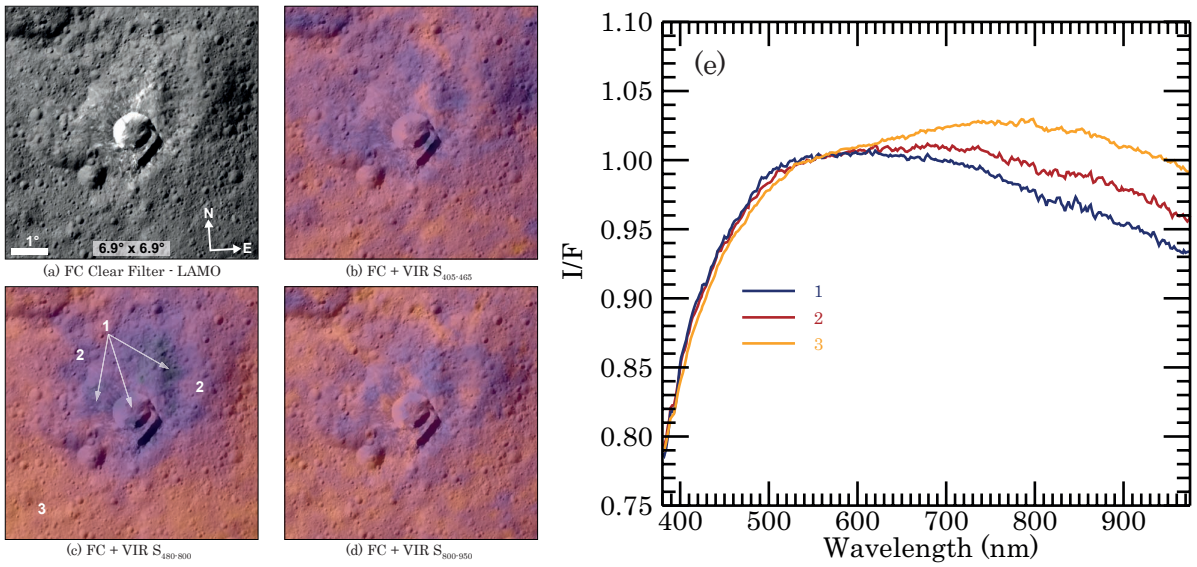

Fig. 14. Same as Fig. 8 for Oxo. Oxo has a diameter of 10 km. All the images use a spherical projection with a field of 6.9° × 6.9° and have the same orientation.

5.1. Reflectance and color composites

The $I/F_{550\mathrm{nm}}$ (Fig. 2) map obtained in this study is comparable to the ones discussed by Ciarniello et al. (2017), whose photometric correction is also used for producing the $I/F_{550\mathrm{nm}}$ map presented in Sect. 3.1, and Longobardo et al. (2018), which were also based on the VIR data but with a slightly different dataset and without taking advantage of the new slope correction presented in Sect. 2.2. The VIS and the IR reflectance are relatively similar but some differences may be noted (Ciarniello et al. 2017; Frigeri et al. 2019). In Ciarniello et al. (2017), an albedo difference map between the $I/F_{550\mathrm{nm}}$ and the $I/F_{2\mu\mathrm{m}}$ was shown and some areas like Haulani, Occator, and Oxo appear brighter in the VIS than in the IR. Among them, Haulani is the most evident, which can be recognized directly in the IR albedo map, being characterized by IR-dark ejecta. For the others, such differences are more subtle. These VIS-IR comparisons also apply to the $I/F_{550\mathrm{nm}}$ map presented in the study (Fig. 2). This latter shows very good qualitative agreement with the maps produced by Nathues et al. (2016), Schröder et al. (2017) and Li et al. (2019) based on the Framing Camera observations; small differences may be due to a different approach in the photometric correction and we do not discuss this here.

The RGB (Fig. 3) and the RGB ratio (Fig. 4) composites allow for much more information to be highlighted than in the reflectance map, which only reveals only the variation of albedo. The bands of the RGB composites have been chosen to correspond to the ones of Nathues et al. (2016) and Schröder et al. (2017), who have worked with the data of the Framing Camera; thus, the results are very similar, in particular with regard to the maps presented by Schröder et al. (2017). The RGB composite map of Sect. 3.2, Fig. 3, is also comparable to the one presented by Ciarniello et al. (2017), but it takes advantage of the correction developed by Rousseau et al. (2019) and is based on a more complete dataset.

The first RGB composite of Ceres (Fig. 3) only allows us to distinguish the most important color and albedo variations. Such albedo differences are visible between the bright Vendimia Planitia and dark Hanami Planum; between the north and the south of Dantu (bright and dark, respectively) or between the northeast of Occator (very dark ejecta) and the Juling and Kupalo region (very bright), for example. The color variability, as appearing in our composite, span between the bluest craters like Haulani, Occator (except the faculae), Ikapati, Centeotl, or Tawals, and the red areas like the Occator facula, the Juling crater floor, the central peak of Urvara and the surroundings of Ernutet while the major part of the surface is displayed as grey-beige. The Occator Cerealia faculae and the Ernutet surroundings are the reddest places on the Ceres surface. In the latter case, organic-rich material has been identified by De Sanctis et al. (2017). More rarely, green-blue colors are observed, like at Ahuna Mons (which appears greener than blue as mentioned by Schröder et al. 2017) or Xevioso. Dantu northern ejecta displays a deeper green color. This deep green is not visible elsewhere, highlighting the dichotomy observed on the Dantu crater and ejecta, as already noted in Fig. 3. At a local scale, some of the VIS bright features are bluish. However, we do not observe a clear correlation between the albedo and the color at global scale, neither directly in the first RGB composite (Fig. 3) nor by comparing the $I/F_{550\mathrm{nm}}$ and the RGB ratio maps (Figs. 2 and 4).

5.2. Slopes

Spectral slopes are not fully diagnostic of surface composition, as opposed to absorption bands. They instead give clues about a number of factors by which they are influenced, such as: (1) the variation of the composition; (2) the grain size (e.g., Adams & Filice 1967; Britt et al. 1992); (3) the structure of the sample and the mixing modalities when several species coexist in a powder or a regolith (e.g., Cloutis et al. 2011, 2012; Poch et al. 2016; Rousseau et al. 2018); (4) the space weathering effects (e.g., Moroz et al. 2004; Nesvorný et al. 2005; Lazzarin et al. 2006; Lucey & Riner 2011; Lantz et al. 2013).

These various processes serve as possible explanations for the spectral slope variations observed by VIR in the VIS on the surface of Ceres. It is not the purpose of this study to discuss each one in detail, however, in the following sections, when applicable, we consider whether one or several of these processes can be favored as an explanation of our observations. The three main spectral slopes that we defined for Ceres in the VIS show

marked changes, as shown in the various maps of Sect. 3. We notice that $S_{480-800nm}$ brings out most of the information. The slope $S_{800-950nm}$ highlights almost the same surface features but with less clarity. This is partly explained by the larger wavelength range used to define the $S_{480-800nm}$ slope, which allows for sharpening the variations. However, it does not rule out that particular processes acting on the surface may be preferably visible in that range. For its part, the $S_{800-950nm}$ can be impacted by the same factors – then toward the VIS wavelengths – while we cannot exclude that the broad absorption band present around 1.1 μm (Rivkin et al. 2011; De Sanctis et al. 2015; Raponi et al. 2019c) plays also a role if it varies across the surface. As described in the previous sections, the $S_{480-800nm}$ and the $S_{800-950nm}$ slopes mainly highlight the features related to impact craters and their ejecta. As discussed below, this generally corresponds to the "blue" material as mentioned by Nathues et al. (2016), Stephan et al. (2017) and Schröder et al. (2017). Because of their peculiar composition, only a couple of exceptions behave differently and show positive slope (or less negative for $S_{800-950nm}$). This is the case for the material present at Ernutet, Urvara's central peak, and the Occator faculae. We also observe several crater floors showing the same positive slopes (Juling, Braciaca, Cacaguat and an unnamed crater north of Haulani (7.7°E-20.7°N)), while the others do not. Those crater floors also exhibit a red color in the RGB ratio. This peculiar behavior (also visible as a red color in the RGB ratio map, also noted by Stephan et al. 2017) is observed only for few craters and argues for a difference in the composition of the crater floor. Frigeri et al. (2019) report the variations of the spectral slopes between 1.163 and 1.891 μm and between 1.891 and 2.250 μm. The $S_{480-800nm}$ and the $S_{800-950nm}$ slopes follow roughly the same trend observed in the IR spectral slopes. This suggests that the factors involved in the variations of the spectral slopes induce the same behavior from the visible to the near-infrared.

The $S_{405-465nm}$ slope can also be affected by the same processes that act on the $S_{480-800nm}$ and $S_{800-950nm}$ slopes. However, its behavior is very distinct, and the spectrum of Ceres in this range experiences an important drop toward the UV. This means that other surface properties can be monitored through this spectral indicator. Absorptions due to crystal field effects, conduction bands, (intervalence) charge transfers, and color centers (or F-centers) may occur at these wavelengths (Hunt 1977; Sherman et al. 1982; Burns 1989; Clark 1999). However, crystal field effects bands are generally narrow (with respect to charge transfer in Fe or Fe–O), and these processes are certainly not responsible for the absorption (Hunt 1977; Clark 1999). On the other hand, conduction bands, while envisaged by Hendrix et al. (2016) based on *Hubble* Space Telescope observations of Ceres, have a sharp edge toward the visible (Johnson & Fanale 1973), which seems to be incompatible with what we observed with VIR. In addition, they occur in minerals that are neither expected (e.g., sulfur compounds, Hunt 1977), nor have been observed on Ceres so far. Finally, absorptions linked to color centers occur in bright minerals (e.g., sulfur, quartz, sodium chloride), but the presence and eventually the quantity needed to be responsible of the absorption observed in the VIR VIS spectra is not compatible with the global reflectance level of Ceres. On the contrary, the band attributed to a charge transfer is common in terrestrial minerals, with its band center is located in the UV with the long-wavelength edge occurring in the VIS; charge transfer absorptions are typically hundreds to thousands of times stronger than the crystal fields bands. Considering that, two processes may cause an absorption compatible with the range of the VIR observations. The first would be the charge-transfer between iron and oxygen, $O_2^- \longrightarrow Fe^{3+}$ (Sherman et al. 1982), which could be linked, on Ceres, to the presence of a Fe-bearing phyllosilicate (e.g., antigorite), or at the presence of the magnetite; all being present or potentially present on the surface (Rivkin et al. 2011; De Sanctis et al. 2015). The second would be the metal-to-metal charge-transfer transition, which could be schematized as $2\,Fe^{3+} \longrightarrow Fe^{2+} + Fe^{4+}$ (Kennedy & Frese 1978), which causes an absorption feature in the same range. This latter charge-transfer could occur by starting with the oxidation of the serpentine which leads to a degradation of the mineral structure and to an augmentation of the Fe^{3+} in this structure. Finally, the charge transfer, compatible with the drop observed in Ceres' spectrum before 500 nm, may experience variations on the surface. In that case, the deeper the band, the steeper the $S_{405-465nm}$, which then would be a proxy of these processes and consequently of the abundance of the host mineral(s).

5.3. The blue material

While not specific to Ceres (Jaumann et al. 2008), terrains with negative spectral slopes compared to the Ceres average have been noted by Nathues et al. (2016), Schröder et al. (2017) and Stephan et al. (2017) over the Framing Camera range. The bluish regions on Ceres' surface are clearly visible in the ratio of images acquired by the FC using filters centered at the wavelengths 438 and 749 nm, the F8 and F3 filters, respectively (Stephan et al. 2017). Schmedemann et al. (2016) also show the existing age-dependency observed between the blue material and the age of the surface, with the bluest being the youngest. The RGB ratio and the $S_{480-800nm}$ maps (Figs. 4 and 6) show a similar spectral behavior than what is observed with the FC. Indeed, a majority of craters and ejecta, as well as few geological features of endogenous origin (e.g., Ahuna Mons) appear bluer than the globally red surface. In parallel to the FC images, Stephan et al. (2017) made use of the VIR infrared data to confirm the observed blueing. Here, we confirm this observation thanks to the corrected VIR visible data.

The origin of the blueing is thoroughly discussed in Stephan et al. (2017), who favor a change in particle sizes or an amorphization of the phyllosilicates (with other materials not excluded) to explain this spectral behavior. On the other hand, due to the presence of water-ice in the subsurface of Ceres (Prettyman et al. 2016; Hiesinger et al. 2016), Schröder et al. (2017) favor a process similar to what Poch et al. (2016) produced in the laboratory, that is, blue spectral behavior of an intra-mixture of smectite and water ice, even after the sublimation of the water ice. In that case, the blueing is due to the foam-like structure of the residue (Poch et al. 2016). This latter explanation, which has been reproduced with a Ceres-like mixture by Schröder et al. (2019, 2020) is not favored by Stephan et al. (2017) because of the possible difficulty in keeping the water-ice stable in the ejecta during the impact process and the ejecta deposition. We suggest that the two explanations are not incompatible. The scenario of Schröder et al. (2017, 2019) could be more likely in the vicinity of the craters. Indeed, lobate flows and knobby crater floors are observed across Ceres (Buczkowski et al. 2016). The solutions put forward by Stephan et al. (2017) could play a role on the ejecta, whatever its distance to the crater, explaining why even the farthest exhibits a blue color and spectral slope. The observations of ejecta, like the ones of Haulani or Oxo, where a distinct ejecta blanket is observed close to the crater and is associated with a very blue color and low $S_{480-800nm}$ slope, while the rest of the ejecta are farther and less blue (see Sects. 4.4 and 4.7), support this.

Over time, the Ceres surface tends to become redder due to the combination of various processes, such as impact gardening, space weathering, and changes in the surface physical properties, such as grain size (Schmedemann et al. 2016; Stephan et al. 2017; Schröder et al. 2017). The current result, as observed by the FC and the VIR in the visible, is a globally red Ceres surface that is punctuated by the blue material coming from the most recent impacts and by some endogenous processes.

5.4. Comparison with the VIR infrared composition maps

The global mapping of Ceres in the infrared revealed a widespread abundance of phyllosilicates (De Sanctis et al. 2015; Ammannito et al. 2016) and Mg-carbonates with localized spots of Na-carbonates (De Sanctis et al. 2016; Carrozzo et al. 2018; see also McCord et al. (2019) for further references).

5.4.1. Phyllosilicates

The Mg– and NH_4- phyllosilicate maps of Ammannito et al. (2016) have a similar general trend but present small differences. We observe that the variations of the $S_{480-800nm}$ qualitatively follow one of the Mg-phyllosilicate abundances: where the abundances of the Mg-phyllosilicate are lower (e.g., Haulani, Ikapati, south Dantu, Occator, Juling, and Kupalo), the $S_{480-800nm}$ slope is also lower. Some exceptions can be noted, such as for Ernutet and Urvara.

Contrary to $S_{480-800nm}$, $S_{405-465nm}$ is more similar to the NH_4-phyllosilicate map. In particular, within the Vendimia Planitia region and close to the Urvara central peak, $S_{405-465nm}$ is steeper and the NH_4-phyllosilicates are more abundant, following Ammannito et al. (2016). However, the opposite behavior is observed for the crater centered at 138°E–24°S: $S_{405-465nm}$ is higher but De Sanctis et al. (2019) report a lower abundance of phyllosilicates.

5.4.2. Carbonates

Carbonates are globally present on Ceres as Mg-carbonates and in localized spots associated with impact craters, fractures, cryovolcanic structures, or bright spots as Na-carbonates (De Sanctis et al. 2016; Zambon et al. 2017; Carrozzo et al. 2018). The global distribution of Mg-carbonates, which is very homogeneous, does not correlate with the behavior of the VIS spectrum through the various spectral parameters investigated in Sect. 3.

Concerning Na-carbonates, a high abundance is observed in Occator faculae (De Sanctis et al. 2016) and Urvara (eastern rim and central peak), matching a larger $S_{405-465nm}$. However, this trend is not observed in Ahuna Mons (Fig. 8), Ikapati, Oxo (Fig. 14), Azacca, Ernutet (Fig. 10), or Haulani (Fig. 11), where Na-carbonates are also safely identified (Carrozzo et al. 2018). On their side, the $S_{480-800nm}$ and the $S_{800-950nm}$ slopes show bluer behavior when Na-carbonates are present (except for Ernutet and the Urvara central peak), but an equal trend is observed in very different locations, as well as when Na-carbonates are absent. Thus, no direct correlations exist between spectral slopes and carbonates.

Regarding the RGB ratio composite, we may observe a distinct green-blue color in certain areas where Na-carbonates are detected. This is the case for Ahuna Mons, Xevioso, an unnamed crater in the northeast of Xevioso (located at 318°E-8.7°N and designed as "crater 1" by Carrozzo et al. 2018), and, to a lesser extent, for Kupalo. However, the trend is not always the same: for example, Kupalo is rich in Na-carbonates but only mildly green-blue in the RGB ratio composite. On the contrary, the Cacaguat crater appears green-blue in the RGB ratio composite but no Na-carbonates seems to be detected on the map presented by Carrozzo et al. (2018). Since the VIS color is driven by different processes, other locations with a green-blue color in Fig. 4 and associated with already existing carbonates could be masked because of the dominance of the blue color – corresponding to the fresh material excavated from the crater – or because of a lower abundance of carbonates or, finally, because of various surface properties. Thus, this correlation is not obvious and is not observed for all Na-carbonates-rich areas. Tosi et al. (2018) and Carrozzo et al. (2018) show that a process of dehydration could happen for various hydrated Na-carbonate species.It may be speculative but if a link exists between the green-blue color and the carbonates, its origin could possibly be found through this process.

6. Conclusion

Using the newly corrected VIR VIS dataset of Ceres (Rousseau et al. 2019), we characterized its surface in the visible by means of various spectral parameter maps. Our maps have been made available for the community through the Aladin Desktop software. Our spectral parameters highlight marked and distinct changes at both global and local scales, testifying to variations in the composition and in the physical properties of the Ceres' surface.

We show that the main driver of the changes in the color and of the $S_{480-800\,nm}$ spectral slope (and to a lesser extent, $S_{800-950nm}$) are the impact craters, which tend to turn the crater floors and the ejecta blue. This has already been noticed in Framing Camera observations (Nathues et al. 2016; Stephan et al. 2017; Schröder et al. 2017). We observe some exceptions, such as north of Dantu and various red crater floors (e.g., Juling), indicating that differences in the surface properties may occur there. Features of endogenous origin may be bluer (e.g., Ahuna Mons) or redder (Occator faculae) than the global Ceres surface. As already observed, the organic material at Ernutet appears red through the $S_{480-800nm}$ and the $S_{800-950nm}$ spectral slopes, but is not outlined by the $S_{405-465\,nm}$.

The $S_{405-465nm}$ spectral slope characterizes the drop of the Ceres spectrum observed toward the UV. We suggest that the $O_2^- \longrightarrow Fe_3^+$ and/or the $2Fe^{3+} \longrightarrow Fe^{2+} + Fe^{4+}$ charge transfer may be responsible for this absorption and that the $S_{405-465nm}$ slope could be a proxy to follow its variations. However, no mineral phases can be identified on the unique basis of the visible data. The $S_{405-465\,nm}$ slope presents other behaviors compared to $S_{480-800\,nm}$ and $S_{800-950\,nm}$ slopes, evidencing different surface features (crater and ejecta are less visible compared to $S_{480-800\,nm}$ slope). In particular, the north of Dantu is well highlighted as in the RGB composite maps. The $S_{405-465\,nm}$ and RGB ratio characteristics at Dantu therefore suggest that the Dantu region may differ, in terms of composition and surface physical properties, compared to the rest of the surface of Ceres.

At visible wavelengths, beyond 550 nm, the Ceres visible spectrum is devoid of absorption bands. This implies that no mineral species with a signature in the visible are identified. If present, they exist in a small amount and the dark phase of the surface may mask them easily. We compared the abundance maps of the phyllosilicates and carbonates with the visible parameters of this study. We observed some correlations between the Mg-phyllosilicates and the slope, $S_{480-800nm}$, and between the NH_4-phyllosilicates and the slope, $S_{405-465nm}$. In the latter case, the correlation is particularly strong in the Dantu region.

Concerning the carbonates, no correlation exists between visible spectral parameters and the Mg-carbonates. We observe a partial correlation between the distribution of the Na-carbonates and the VIS spectral slopes and color. However, the variations of the VIS slopes cannot be attributed to their presence alone.

Acknowledgements. VIR is funded by the Italian Space Agency (ASI) and was developed under the leadership of INAF-Istituto di Astrofisica e Planetologia Spaziali, Rome, Italy (Grant ASI INAF I/004/12/0). The instrument was built by Selex-Galileo, Florence, Italy. The authors acknowledge the support of the Dawn Science, Instrument, and Operations Teams. The authors made use of TOPCAT (Tools for OPerations on Catalogues And Tables, Taylor 2005) for a part of the data analysis and figure production. This research has made use of "Aladin Desktop" developed at CDS, Strasbourg Observatory, France (Bonnarel et al. 2000; Fernique et al. 2015). We thank Sharon Uy (UCLA, USA), who greatly helped for manuscript editing. We thank the anonymous reviewer for the insightful suggestions which improved the paper.

References

Adams, J. B., & Filice, A. L. 1967, J. Geophys. Res., 72, 5705
Ammannito, E., DeSanctis, M. C., Ciarniello, M., et al. 2016, Science, 353, aaf4279
Beran, A. 2002, Rev. Mineral. Geochem., 46, 351
Bishop, J. L., Dobrea, E. Z. N., McKeown, N. K., et al. 2008, Science, 321, 830
Bonnarel, F., Fernique, P., Bienaymé, O., et al. 2000, A&AS, 143, 33
Britt, D., Bell, J., Haack, H., & Scott, E. 1992, Lunar Planet. Sci. Conf., 23, 167
Buczkowski, D. L., Schmidt, B. E., Williams, D. A., et al. 2016, Science, 353, aaf4332
Buczkowski, D., Williams, D., Scully, J., et al. 2018, Icarus, 316, 128
Burns, R. G. 1989, Mineral. Mag., 53, 135
Bus, S. J., & Binzel, R. P. 2002a, Icarus, 158, 146
Bus, S. J., & Binzel, R. P. 2002b, Icarus, 158, 106
Carrozzo, F. G., Raponi, A., De Sanctis, M. C., et al. 2016, Rev. Sci. Instrum., 87, 124501
Carrozzo, F. G., De Sanctis, M. C., Raponi, A., et al. 2018, Sci. Adv., 4, e1701645
Carry, B., Dumas, C., Fulchignoni, M., et al. 2008, A&A, 478, 235
Chapman, C. R., & Gaffey, M. J. 1979, Asteroids, eds. T. Gehrels, & M. S. Matthews (Tucson, AZ: University of Arizona Press), 655
Ciarniello, M., Capaccioni, F., Filacchione, G., et al. 2015, A&A, 583, A31
Ciarniello, M., Sanctis, M. C. D., Ammannito, E., et al. 2017, A&A, 598, A130
Clark, R. 1999, Remote Sensing for the Eartb Sciences: Manual of Remote Sensing, ed. Rencz, A. N. (New York: John Wiley and Sons, Inc), 3
Cloutis, E., Hiroi, T., Gaffey, M., Alexander, C., & Mann, P. 2011, Icarus, 212, 180
Cloutis, E. A., Hudon, P., Hiroi, T., Gaffey, M. J., & Mann, P. 2012, Icarus, 221, 984
Combe, J.-P., McCord, T. B., Tosi, F., et al. 2016, Science, 353, aaf3010
Combe, J.-P., Raponi, A., Tosi, F., et al. 2019, Icarus, 318, 22
Crown, D. A., Sizemore, H. G., Yingst, R. A., et al. 2018, Icarus, 316, 167
De Sanctis, Coradini, A., Ammannito, E., et al. 2011, Space Sci. Rev., 163, 329
De Sanctis, M.-C., Capaccioni, F., Ciarniello, M., et al. 2015, Nature, 525, 500
De Sanctis, M. C., Raponi, A., Ammannito, E., et al. 2016, Nature, 536, 54
De Sanctis, M. C., Ammannito, E., McSween, H. Y., et al. 2017, Science, 355, 719
De Sanctis, M. C., Ammannito, E., Carrozzo, F. G., et al. 2018a, Meteorit. Planet. Sci., 53, 1844
De Sanctis, M. C., Vinogradoff, V., Raponi, A., et al. 2018b, MNRAS, 482, 2407
De Sanctis, M., Frigeri, A., Ammannito, E., et al. 2019, Icarus, 318, 230
De Sanctis, M. C., Ammannito, E., Raponi, A., et al. 2020, Nat. Astron., 4, 786
Fernique, P., Allen, M. G., Boch, T., et al. 2015, A&A, 578, A114
Frigeri, A., De Sanctis, M., Ammannito, E., et al. 2019, Icarus, 318, 14
Hapke, B. 2012, Theory of Reflectance and Emittance Spectroscopy (Cambridge: Cambridge University Press)
Hendrix, A. R., Vilas, F., & Li, J.-Y. 2016, Geophys. Res. Lett., 43, 8920
Hiesinger, H., Marchi, S., Schmedemann, N., et al. 2016, Science, 353, aaf4758
Hunt, G. R. 1977, Geophysics, 42, 501
Jaumann, R., Stephan, K., Hansen, G., et al. 2008, Icarus, 193, 407
Johnson, T. V., & Fanale, F. P. 1973, J. Geophys. Res., 78, 8507
Kennedy, J. H., & Frese, K. W. J. 1978, J. Electrochem. Soc., 125, 709
Kneissl, T., Schmedemann, N., Neesemann, A., et al. 2016, Lunar Planet. Sci. Conf., 47, 1967
Krohn, K., Jaumann, R., Otto, K., et al. 2018, Icarus, 316, 84
Lantz, C., Clark, B. E., Barucci, M. A., & Lauretta, D. S. 2013, A&A, 554, A138
Lawrence, D. J., Peplowski, P. N., Beck, A. W., et al. 2018, Meteorit. Planet. Sci., 53, 1805
Lazzarin, M., Marchi, S., Moroz, L. V., et al. 2006, ApJ, 647, L179
Lazzaro, D., Ferraz-Mello, S., & Fernández, J. A. 2006, Asteroids, comets, meteors, IAU Symp. 229 (Cambridge: Cambridge University Press)
Li, J.-Y., McFadden, L. A., Parker, J. W., et al. 2006, Icarus, 182, 143
Li, J.-Y., Schröder, S. E., Mottola, S., et al. 2019, Icarus, 322, 144
Longobardo, A., Palomba, E., Galiano, A., et al. 2018, Icarus, 320, 97
Lucey, P. G., & Riner, M. A. 2011, Icarus, 212, 451
Marchi, S., Ermakov, A. I., Raymond, C. A., et al. 2016, Nat. Commun., 7, 12257
McCord, T., Zambon, F., Russell, C., & Raymond, C. 2019, Icarus, 318, 1
Moroz, L., Arnold, G., Korochantsev, A., & Wasch, R. 1998, Icarus, 134, 253
Moroz, L., Baratta, G., Strazzulla, G., et al. 2004, Icarus, 170, 214
Nathues, A., Hoffmann, M., Platz, T., et al. 2016, Planet. Space Sci., 134, 122
Nesvorný, D., Jedicke, R., Whiteley, R. J., & Ivezić, Ž. 2005, Icarus, 173, 132
Palomba, E., Longobardo, A., Sanctis, M. D., et al. 2019, Icarus, 320, 202
Parker, J. W., Stern, S. A., Thomas, P. C., et al. 2002, AJ, 123, 549
Pieters, C. M., Nathues, A., Thangjam, G., et al. 2017, Meteorit. Planet. Sci., 53, 1983
Platz, T., Nathues, A., Sizemore, H., et al. 2018, Icarus, 316, 140
Poch, O., Pommerol, A., Jost, B., et al. 2016, Icarus, 267, 154
Prettyman, T. H., Feldman, W. C., McSween, H. Y., et al. 2011, Space Sci. Rev., 163, 371
Prettyman, T. H., Yamashita, N., Toplis, M. J., et al. 2016, Science, 355, 55
Preusker, F., Scholten, F., Matz, K.-D., et al. 2016, Lunar Planet. Sci. Conf., 47, 1954
Raponi, A., De Sanctis, M. C., Frigeri, A., et al. 2018, Science Advances, 4, eaao3757
Raponi, A., De Sanctis, M., Carrozzo, F., et al. 2019a, Icarus, 320, 83
Raponi, A., Carrozzo, F., Zambon, F., et al. 2019b, Icarus, 318, 99
Raponi, A., Ferrari, M., De Sanctis, M. C., et al. 2019c, 13, EPSC
Rivkin, A. S., Li, J.-Y., Milliken, R. E., et al. 2011, Space Sci. Rev., 163, 95
Roatsch, T., Kersten, E., Matz, K. D., et al. 2016a, Dawn FC2 Derived Ceres Mosaics V1.0
Roatsch, T., Kersten, E., Matz, K.-D., et al. 2016b, Planet. Space Sci., 129, 103
Roettger, E., & Buratti, B. 1994, Icarus, 112, 496
Rousseau, B., & Érard, S. 2019, EPSC-DPS2019 No. 514
Rousseau, B., Érard, S., Beck, P., et al. 2018, Icarus, 306, 306
Rousseau, B., Raponi, A., Ciarniello, M., et al. 2019, Rev. Sci. Instrum., 90
Ruesch, O., Platz, T., Schenk, P., et al. 2016, Science, 353, aaf4286
Ruesch, O., Genova, A., Neumann, W., et al. 2019, Nat. Geosci., 12, 505
Russell, C. T., Capaccioni, F., Coradini, A., et al. 2007, Earth Moon Planets, 101, 65
Schenk, P., Sizemore, H., Schmidt, B., et al. 2018, Icarus, 320, 159
Schmedemann, N., Kneissl, T., Neesemann, A., et al. 2016, Geophys. Res. Lett., 43, 11
Schröder, S., Mottola, S., Carsenty, U., et al. 2017, Icarus, 288, 201
Schröder, S. E., Poch, O., Ferrari, M., et al. 2019, 13, EPSC
Schröder, S. E., Poch, O., Ferrari, M., et al. 2020, Nat. Commun., submitted
Scully, J. E., Bowling, T., Bu, C., et al. 2019, Icarus, 320, 213
Sherman, D. M., Burns, R. G., & Mee Burns, V. 1982, J. Geophys. Res., 87, 10 169
Sierks, H., Keller, H. U., Jaumann, R., et al. 2011, Space Sci. Rev., 163, 263
Stein, N., Ehlmann, B., Palomba, E., et al. 2019, Icarus, 320, 188
Stephan, K., Jaumann, R., Krohn, K., et al. 2017, Geophys. Res. Lett., 44, 1660
Stephan, K., Jaumann, R., Wagner, R., et al. 2018, Meteorit. Planet. Sci., 53, 1866
Stephan, K., Jaumann, R., Zambon, F., et al. 2019, Icarus, 318, 111
Taylor, M. B. 2005, ASP Conf. Ser., 347, 29
Tosi, F., Carrozzo, F. G., Raponi, A., et al. 2018, Meteorit. Planet. Sci., 53, 1902
Tosi, F., Carrozzo, F., Zambon, F., et al. 2019, Icarus, 318, 170
Williams, D. A., Kneissl, T., Neesemann, A., et al. 2018, Icarus, 316, 99
Zambon, F., Raponi, A., Tosi, F., et al. 2017, Geophys. Res. Lett., 44, 97
Zambon, F., Carrozzo, F., Tosi, F., et al. 2019, Icarus, 318, 212

Appendix A: Density maps

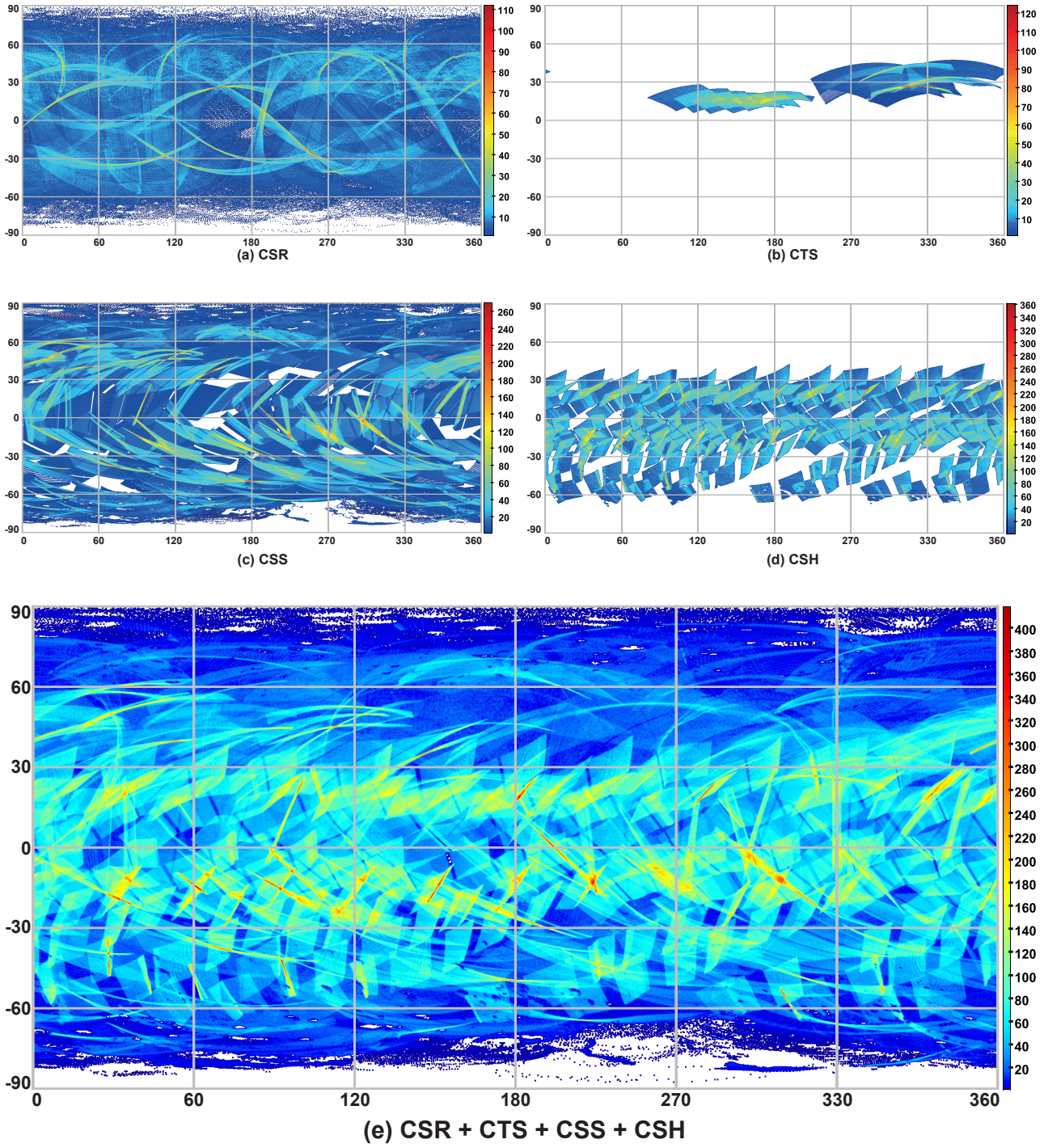

Fig. A.1. Density maps of the VIR visible data set used in the study. *Panel A*: CSR mission phase; *panel B*: CTS; *panel C*: CSS; *panel D*: CSH; and *panel E*: regroups every four. For details about the mission phases, see Table 1 and Sect. 2.2. Each map is built with TOPCAT with a Plate Carée projection (see Sect. 2.4), and observations are represented as points. The scale corresponds to the square root of the observation density.